Defect formation in $LaGa(Mg,Ni)O_{3-\delta}$: A statistical thermodynamic analysis validated by mixed conductivity and magnetic susceptibility measurements

E. N. Naumovich,[1,2] V. V. Kharton,[1,2,*] A. A. Yaremchenko,[1] M. V. Patrakeev,[3] D. G. Kellerman,[3] D. I. Logvinovich,[2] and V. L. Kozhevnikov[3]

[1]*Department of Ceramics and Glass Engineering, CICECO, University of Aveiro, 3810-193 Aveiro, Portugal*

[2]*Institute of Physicochemical Problems, Belarus State University, 14 Leningradskaya Strasse, 220050 Minsk, Belarus*

[3]*Institute of Solid State Chemistry, Ural Division of RAS, 91 Pervomayskaya Strasse, 620219 Ekaterinburg, Russia*

(Received 25 April 2006; published 8 August 2006)

A statistical thermodynamic approach to analyze defect thermodynamics in strongly nonideal solid solutions was proposed and validated by a case study focused on the oxygen intercalation processes in mixed-conducting $LaGa_{0.65}Mg_{0.15}Ni_{0.20}O_{3-\delta}$ perovskite. The oxygen nonstoichiometry of Ni-doped lanthanum gallate, measured by coulometric titration and thermogravimetric analysis at 923–1223 K in the oxygen partial pressure range 5×10^{-5} to 0.9 atm, indicates the coexistence of Ni^{2+}, Ni^{3+}, and Ni^{4+} oxidation states. The formation of tetravalent nickel was also confirmed by the magnetic susceptibility data at 77–600 K, and by the analysis of *p*-type electronic conductivity and Seebeck coefficient as function of the oxygen pressure at 1023–1223 K. The oxygen thermodynamics and the partial ionic and hole conductivities are strongly affected by the point-defect interactions, primarily the Coulombic repulsion between oxygen vacancies and/or electron holes and the vacancy association with Mg^{2+} cations. These factors can be analyzed by introducing the defect interaction energy in the concentration-dependent part of defect chemical potentials expressed by the discrete Fermi-Dirac distribution, and taking into account the probabilities of local configurations calculated via binomial distributions.

DOI: 10.1103/PhysRevB.74.064105 PACS number(s): 72.60.+g, 66.10.Ed, 72.80.Ga, 82.60.Lf

I. INTRODUCTION

Mixed oxygen-ion and electron conducting (MIEC) materials are the focus of much interest for application in electrochemical devices, including oxygen sensors, solid oxide fuel cells (SOFCs), and dense ceramic membranes for oxygen separation and conversion of light hydrocarbons. In particular, partial oxidation of methane (POM) to the so-called synthesis gas (syngas), a mixture of hydrogen and carbon monoxide, may take place efficiently on the surface of MIEC membranes integrating oxidation with controlled oxygen separation in a single reactor.[1–3] The simplicity of the system implies significant savings in energy and capital compared to the conventional syngas production method of steam reforming of methane. Commercialization of the membrane reactors, however, requires achieving the often incompatible aims of high oxygen permeation fluxes, chemical stability, and moderate thermal and chemical induced expansion for both oxidizing and reducing conditions. These requirements limit the applicability of numerous MIECs with highest oxygen permeability, such as perovskite-related $(Sr,La)(Fe,Co)O_{3-\delta}$ which exhibit thermodynamic and dimensional instability under high oxygen chemical potential gradients.[4,5]

One promising group of membrane materials is the perovskite-type systems based on lanthanum gallate.[3,5–9] Undoped $LaGaO_3$ is an insulator with the total conductivity as low as 6×10^{-5} $S\times cm^{-1}$ at 1223 K in air.[10] The substitution of lanthanum with alkaline-earth metals (Ca, Sr, or Ba) or gallium with divalent metal cations (such as Mg or Ni) increases oxygen vacancy concentration and, consequently, ion diffusivity.[11–14] For $LaGaO_3$ derivatives with predominant ionic transport, the highest level of conductivity (0.13–0.17 $S\times cm^{-1}$ at 1073 K) is observed for $La_{1-x}Sr_xGa_{1-y}Mg_yO_{3-\delta}$ (LSGM) solid solutions where $x=0.10-0.20$ and $y=0.15-0.20$.[11–13] The incorporation of alkaline-earth metal cations with relatively large radii may however decrease the membrane stability, particularly due to interaction with gaseous species such as water vapor,[15] and to an enhanced volatilization of gallium oxide from the ceramics bulk in hydrogen environment.[16] The significant increase in the electronic conduction can be achieved incorporating >10% transition metal cations in the gallium sublattice.[17–21] Electronic transport in $La(Sr)Ga(Mg,M)O_{3-\delta}$ phases containing 15–40 % transition metal dopants occurs via a small-polaron mechanism and increases in the sequence $M=Cr<Mn<Fe<Co\leqslant Ni$.[19–22] The ionic conductivity follows, in general, a similar trend with a maximum for Ni-containing ceramics.[6,8,20–22] Oxygen permeability of $LaGaO_3$-based mixed conductors is lower compared to $(Sr,La)(Fe,Co)O_{3-\delta}$ with highest ionic transport, but still sufficient for membrane applications.[5–8]

Although information on the redox processes determining stability and transport in heavily-doped gallate mixed conductors is scarce, the available data indicate complex defect formation mechanisms, particularly a significant role of the Coulombic interaction between point defects.[21,23] This makes it necessary to consider the nearest neighborhood properties and the probability of placing a defect in the vicinity of other charged species as the factors influencing defect equilibria. One statistical-thermodynamic model accounting for Coulombic interactions and configurational entropy-related exclusion effects was developed by Ling[24–26] to describe the redox behavior of CeO_2- and $LaCrO_3$-based phases. The latter approach showed, however, rather a limited adequacy, especially in conditions where the deviations from stoichi-

ometry are high.[24–26] In the present work, the site-exclusion concept is enhanced introducing the defect interaction energy. In order to verify the model, the equilibrium oxygen intercalation processes in perovskite-type $LaGa_{0.65}Mg_{0.15}Ni_{0.20}O_{3-\delta}$ are analyzed in the oxygen partial pressure range 5×10^{-5} to 0.9 atm at 973–1223 K. This composition was selected as a prototype $LaGaO_3$-based mixed conductor with dominant hole transport and substantially high oxygen permeability,[8,9,22] where no essential delocalization of the *p*-type electronic charge carriers can be expected due to the relatively low concentration of nickel cations. The data on defect thermodynamics are further used for the analysis of partial hole and oxygen-ion conductivities as function of the oxygen chemical potential.

II. DEFECT THERMODYNAMICS IN MODERATELY DILUTED SYSTEMS

The point defect interactions lead to deviations from the well-known relationship for the chemical potential of a point defect, $\mu(Df_X^z)$, derived from the partition sum[27,28]

$$\mu(Df_X^z) = \mu^0(Df_X^z) + \mu'(Df_X^z) = \mu^0(Df_X^z) + RT\ln a(Df_X^z)$$
$$= \mu^0(Df_X^z) + RT\ln\frac{[Df_X^z]}{[Df_{\max}]-[Df_X^z]}, \quad (1)$$

where $[Df_X^z]$ is the concentration of defects Df_X^z in the X sublattice, z is the charge, $[Df_{\max}]$ is the concentration of sites where these defects can be placed, a is the activity, μ^0 and μ' are concentration-independent and concentration-dependent parts of the chemical potential, respectively. Hereafter, all concentration-related terms are normalized to one formula unit. In the simplest case, Eq. (1) can be modified by expressing $[Df_{\max}]$ as a function of the defect concentration and/or selected external conditions, or by introducing the exclusion coefficient (γ) in the denominator

$$\mu(Df_X^z) = \mu^0(Df_X^z) + RT\ln\frac{[Df_X^z]}{\gamma[Df_{\max}]-[Df_X^z]}. \quad (2)$$

However, such corrections may only be adequate for rather isolated defects in strongly diluted systems. For highly-defective lattices, even when ordering of point defects does not occur, the simple alteration of the number of states may hardly describe deviations from the ideal solution model.

The starting hypothesis used in the present work was that some particular defect configurations cannot be formed due to strong Coulombic repulsion forces, as postulated earlier by Ling.[24–26] Another assumption was that the point-defect energy may be altered due to the presence of other defects in the neighborhood, thus splitting into several levels. The relationship between the defect concentration and chemical potential was described using the discrete Fermi-Dirac distribution

$$[Df_X^z] = \sum_{k=0}^{N_k}\frac{N(Df_X^z,k)}{\exp\left[\dfrac{(E_k^0+E_k)-\mu(Df_X^z)}{RT}\right]+q_n}, \quad (3)$$

where $N(Df_X^z,k)$ is the number of states on the kth level, E_k is the energy of this level given with respect to the ground level E_k^0, and q_n is a spin-determined constant (in the present case $q_n=1$). The values of E_k can be calculated summing the contributions from all surrounding species; E_k^0 is composition independent for the given phase and, therefore, can be taken equal to $\mu^0(Df_X^z)$. The discrete density of states is to be assessed statistically, by analyzing the probability of different configurations in the defect neighborhood for a fixed overall composition of the lattice. If a lattice element Nh_Y^n placed in the same or another sublattice (Y) affects the chemical potential of Df_X^z species having the k-level energy, the corresponding probability term is expressed via the binomial distribution

$$P(Df_X^z,Nh_Y^n,m) = \binom{N_{YX}}{m}\left(\frac{[Nh_Y^n]}{[Y_{\max}]}\right)^m\left(1-\frac{[Nh_Y^n]}{[Y_{\max}]}\right)^{N_{YX}-m}, \quad (4)$$

where N_{YX} is the coordination number, n is the charge of Nh_Y^n species, m is their number in the neighborhood, $\binom{N_{YX}}{m}$ is the binomial coefficient, and $[Y_{\max}]$ is the number of Y sites per unit formula. If the presence of Nh_Y^n species near Df_X^z is improbable, Eq. (4) simplifies to

$$P(Df_X^z,Nh_Y^n,0) = \binom{N_{YX}}{0}\left(\frac{[Nh_Y^n]}{[Y_{\max}]}\right)^0\left(1-\frac{[Nh_Y^n]}{[Y_{\max}]}\right)^{N_{YX}}$$
$$= \left(1-\frac{[Nh_Y^n]}{[Y_{\max}]}\right)^{N_{YX}}. \quad (5)$$

As this exclusion effect should be symmetrical

$$P(Nh_Y^n,Df_X^z,0) = \left(1-\frac{[Df_X^z]}{[X_{\max}]}\right)^{N_{XY}}. \quad (6)$$

The total number of states for a kth level can be calculated as the product of partial probabilities

$$N(Df_X^z,k) = [Df_{\max}]\times\prod P(Df_X^z,\ldots,\ldots). \quad (7)$$

Substituting Eq. (1) into Eq. (3), the relationship between the concentration and activity may be written as

$$[Df_X^z] = \sum_{k=0}^{N_k}\frac{N(Df_X^z,k)}{\exp\left[\dfrac{E_k-RT\ln a(Df_X^z)}{RT}\right]+1}$$
$$= a(Df_X^z)\sum_{k=0}^{N_k}\frac{N(Df_X^z,k)}{\exp\left[\dfrac{E_k}{RT}\right]+a(Df_X^z)}, \quad (8)$$

where the nominator of the right term is determined by Eq. (7). This equation was used to analyze the concentrations of mobile defects (holes and oxygen vacancies) in

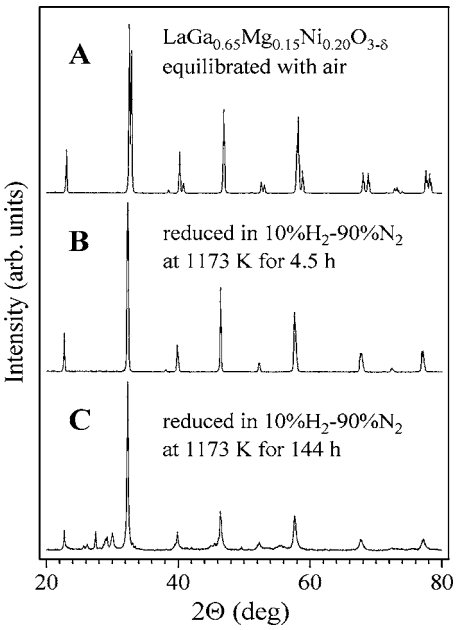

FIG. 1. XRD patterns of $LaGa_{0.65}Mg_{0.15}Ni_{0.20}O_{3-\delta}$ equilibrated with air (a) and reduced in 10%H_2-90%N_2 flow at 1173 K during 4.5 h (b) and 144 h (c).

$LaGa_{0.65}Mg_{0.15}Ni_{0.20}O_{3-\delta}$ lattice as function of the oxygen chemical potential.

III. EXPERIMENT

A. Synthesis and characterization

The powder of $LaGa_{0.65}Mg_{0.15}Ni_{0.20}O_{3-\delta}$ was prepared by the standard solid-state synthesis route from the stoichiometric amounts of high-purity La_2O_3, Ga_2O_3, $Mg(NO_3)_2 \cdot 6H_2O$, and $Ni(NO_3)_2 \cdot 6H_2O$. Prior to weighting, lanthanum and gallium oxides were annealed in air at 1373 K for 3–4 h. After thermal decomposition of nitrates, the solid state reaction was conducted at 1420 to 1620 K during 50 h with multiple intermediate regrinding steps. The powder was ball-milled and pressed at 250–300 MPa; dense ceramic samples were sintered in air at 1798±5 K for 5 h. Then the ceramics were polished, annealed in air at 1273 K for 2 h and slowly furnace cooled in order to achieve equilibrium with air at low temperatures. The powdered samples used for x-ray diffraction (XRD) studies, thermogravimetric analysis (TGA), coulometric titration (CT) and measurements of magnetic susceptibility (χ), were prepared by grinding of dense ceramics.

The experimental techniques and equipment used for general characterization were described elsewhere.[20–23,29–31] The room-temperature XRD analysis (Rigaku D/MAX-B diffractometer, Cu $K\alpha$ radiation) showed formation of single perovskite-type phase, Fig. 1(a); the structure was identified as rhombohedrally-distorted (space group $R\bar{3}c$; unit cell parameters: a_R=0.5466 nm, α_R=60.66°). The density of ceramics was 96.9±0.7% of theoretical density calculated from the XRD data. The ceramic microstructure was characterized by scanning electron microscopy combined with energy-dispersive spectroscopic analysis (SEM/EDS, Hitachi-4100S). No traces of phase segregation at the grain boundaries were detected; the cation distribution along the grains and grains boundaries was found uniform, within the limits of experimental uncertainty of the EDS method. The magnetic susceptibility was studied at 77–600 K by the Faraday method in magnetic fields of 7–10 kOe. The overall cation composition was verified by inductively-coupled plasma (ICP) spectroscopic analysis (Jobin Yvon, model JY 70 plus). The differential thermal analysis (DTA, Setaram LabSys TG-DTA16 instrument) showed no thermal effects on heating up to 1273 K and subsequent cooling in air, thus confirming thermodynamic stability of perovskite-type $LaGa_{0.65}Mg_{0.15}Ni_{0.20}O_{3-\delta}$ phase in the whole temperature range studied in this work.

B. Measurements of electrical properties

The total electrical conductivity (σ, 4-probe dc) and Seebeck coefficient (α) were studied as function of the oxygen partial pressure, $p(O_2)$, varying in the range from 10^{-20} to 0.4 atm at 1023–1223 K. The measurements were performed simultaneously on two bar-shaped ceramic samples placed in yttria-stabilized zirconia (YSZ) solid-electrolyte cell comprising an electrochemical oxygen pump and a sensor; the experimental technique was described elsewhere.[23,29] At the start of the experiment, the cell was evacuated with a vacuum pump, filled with a mixture of O_2 and CO_2 (50:50), and then hermetically sealed. In the course of measurements, the oxygen partial pressure was varied by the solid-electrolyte oxygen pump, continuously pumping oxygen in or out of the cell, and controlled by the sensor. The criteria for equilibration of a sample after a change in either oxygen pressure or temperature included the relaxation rates of the conductivity and Seebeck coefficient less than 0.05 %/min and 0.001 μV/(K×min), respectively.

The oxygen ionic conductivity (σ_O) in air was calculated from the total conductivity and oxygen ion transference numbers (t_O), determined by the faradaic efficiency (FE) technique.[30,31] The FE measurements were carried out at 1023–1223 in air under zero oxygen chemical potential gradient across the sample.

C. Oxygen nonstoichiometry determination

The procedure of TGA (Setaram SetSys 16/18 instrument) included heating up to 1223 K in a flow of dry air, temperature cycling in the range 973–1223 K with a step of 50 K and equilibration at each temperature during 2 h, in order to obtain equilibrium reference points at atmospheric oxygen pressure. Then the apparatus was flushed with argon, followed by reduction in flowing 10%H_2-90%N_2 mixture at 1173 K. The absolute values of oxygen nonstoichiometry (δ) in air were calculated with respect to the point of $LaGa_{0.65}Mg_{0.15}Ni_{0.20}O_{2.825}$ decomposition where all nickel cations are in a 2+ state, determined from the weight relaxation curves (Fig. 2). At this point, $LaGa_{0.65}Mg_{0.15}Ni_{0.20}O_{2.825}$ powder was still single phase, with a larger unit cell volume and a smaller rhombohedral

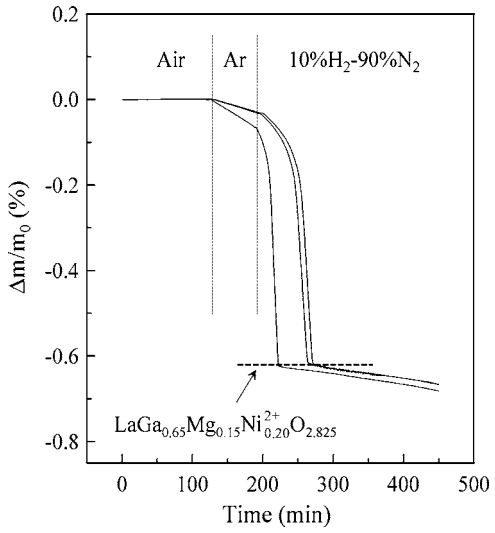

FIG. 2. Determination of the absolute oxygen nonstoichiometry from the weight relaxation curves for three $LaGa_{0.65}Mg_{0.15}Ni_{0.20}O_{3-\delta}$ samples with different weight, at 1173 K. The horizontal dashed line shows the phase decomposition boundary where all nickel is divalent.

distortion compared to the atmospheric oxygen pressure [Fig. 1(b)]. The reproducibility error of δ values in air, estimated in such a manner for three different samples, was ±0.001. Moreover, very similar values were obtained for $LaGa_{0.65}Mg_{0.15}Ni_{0.20}O_{3-\delta}$ powder prepared using alternative synthesis route, namely the glycine-nitrate process.[32] These facts, and the relatively short transient times necessary to achieve the state with δ=0.175, make it possible to neglect possible minor losses of gallium oxide at the initial stage of reduction. Further reduction of $LaGa_{0.65}Mg_{0.15}Ni_{0.20}O_{2.825}$ leads to a continuous decrease in the powder weight (Fig. 3) due to both nickel reduction into metal and gallium oxide volatilization typical for $LaGaO_3$-based materials in H_2-containing atmospheres.[16,33,34] As the latter process is very slow, the use of complete reduction to determine absolute oxygen content in $LaGa_{0.65}Mg_{0.15}Ni_{0.20}O_{3-\delta}$ was impossible. In fact, no time-independent weight can be attained during more than 100–150 h; the overall weight changes were much higher than it might be expected for any oxidation state of nickel if neglecting gallium oxide volatilization. XRD analysis of the sample reduced during 140 h in 10%H_2-90%N_2 flow at 1173 K, showed that the perovskite solid solution is still retained as a major phase, Fig. 1(c).

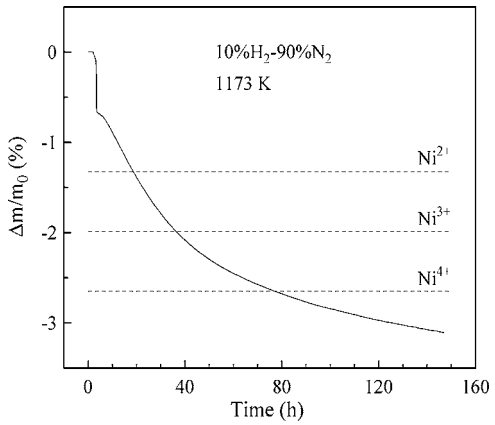

FIG. 3. Relative weight change upon reduction at 1173 K. The sample was equilibrated in air for 2 h, kept in argon for 1 h, and then reduced in 10%H_2-90%N_2 flow for 140 h. Dashed lines correspond to the theoretical weight changes upon reduction into metallic nickel and binary oxides, calculated assuming that there is no gallium oxide volatilization and that all nickel cations in air are in 2+, 3+, or 4+ oxidation states.

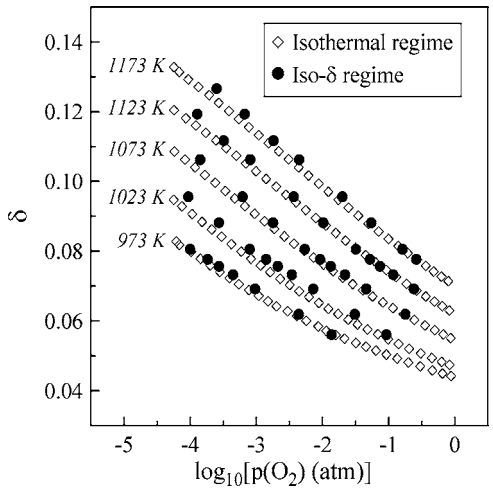

FIG. 4. Reproducibility of the oxygen nonstoichiometry values in $LaGa_{0.65}Mg_{0.15}Ni_{0.20}O_{3-\delta}$, obtained by two different CT techniques.

The oxygen content variation with respect to a reference point at atmospheric oxygen partial pressure were studied at 973–1223 K by two different CT techniques. The first method is the isothermal titration using double electrochemical cells[35] at oxygen pressures from 0.9 atm down to 5×10^{-5}. After each isothermal cycle, reversibility of the redox processes and reproducibility of the results were checked by pumping of oxygen into the cell and remeasuring 3–8 data points. When the complete CT data array under oxidizing conditions was collected, the sample was reduced gradually pumping oxygen out the cell down to phase decomposition at 1223 K; the total change in the oxygen content between atmospheric $p(O_2)$ and the decomposition boundary was in a good agreement with TGA data. For another CT technique,[36] the measurements were performed in the so-called iso-δ regime, varying temperature with the step of 15–25 K and pumping oxygen galvanostatically between temperature cycles. The difference in δ values obtained by two these CT methods at a given temperature and oxygen pressure, was lower than 0.003 (Fig. 4).

IV. RESULTS AND DISCUSSION

A. Nickel oxidation states

Figure 5 presents the oxygen partial pressure dependence of the average nickel oxidation state in perovskite-type $LaGa_{0.65}Mg_{0.15}Ni_{0.20}O_{3-\delta}$, calculated from the data on oxygen nonstoichiometry (Fig. 4) using the crystal electroneu-

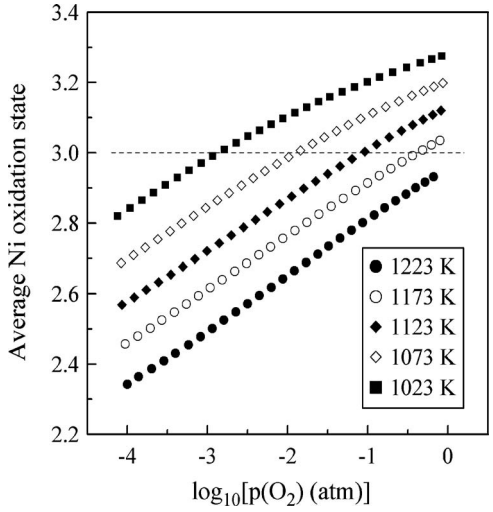

FIG. 5. Oxygen partial pressure dependence of the average oxidation state of nickel cations in $LaGa_{0.65}Mg_{0.15}Ni_{0.20}O_{3-\delta}$, estimated from the oxygen nonstoichiometry data.

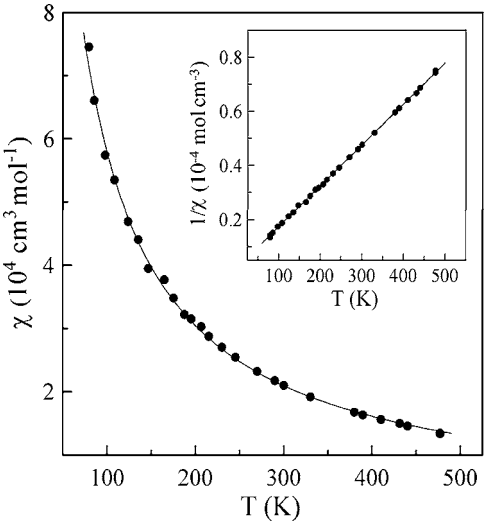

FIG. 6. Magnetic susceptibility of $LaGa_{0.65}Mg_{0.15}Ni_{0.20}O_{3-\delta}$ equilibrated with atmospheric oxygen at low temperatures. Inset illustrates the linear dependence of reciprocal magnetic susceptibility on temperature.

trality condition. These data show coexistence of Ni^{2+}, Ni^{3+}, and Ni^{4+} states in the lattice. At oxygen partial pressures close to 1 atm, the average oxidation state of Ni cations is higher than 3+ even at 1173 K. Note that the formation of tetravalent nickel is rather unusual for perovskite-related nickelates, especially at elevated temperatures. Perovskite-type $LaNiO_{3-\delta}$ is thermodynamically stable at $p(O_2) \leqslant 1$ atm only at temperatures below 1150–1200 K; at higher temperatures this phase decomposes into $La_2NiO_{4+\delta}$ and NiO.[37] In the case of $LaNiO_3$-based solid solutions, the presence of Ni^{4+} was only evidenced by structural and thermogravimetric studies for acceptor-doped $La_{0.9}Sr_{0.1}NiO_{3-\delta}$ prepared at 1273 K under the oxygen pressure of 200 atm.[38] However, tetravalent nickel forms in $La_{2-x}Sr_xNiO_{4-\delta}$ ($x > 1.0$) with perovskite-related K_2NiF_4-type structure synthesized at $p(O_2) = 1$ atm.[39,40] It appears, therefore, that the stabilization of tetravalent nickel in $LaGa_{0.65}Mg_{0.15}Ni_{0.20}O_{3-\delta}$ lattice is achieved due to a relatively diluted state of Ni ions surrounded by the cations with stable valence and a substantially high concentration of acceptor-type Mg^{2+}.

At 77–500 K, $LaGa_{0.65}Mg_{0.15}Ni_{0.20}O_{3-\delta}$ equilibrated at atmospheric oxygen pressure exhibits a paramagnetic behavior (Fig. 6); the temperature dependence of magnetic susceptibility can be adequately described by the Curie-Weiss law. The effective magnetic moment (μ_{eff}^2) of nickel ions, calculated from the fitting results, is equal to 1.67 μ_B^2. Most likely, the magnetic properties of $LaGa_{0.65}Mg_{0.15}Ni_{0.20}O_{3-\delta}$ are determined by a combination of low-spin Ni^{3+} ($\mu^2 = 3\mu_B^2$) and Ni^{4+} ($\mu^2 = 0$), as for deintercalated $Li_xNi_{1-y}Co_yO_2$ system.[41,42] The obtained value of μ_{eff}^2 corresponds, hence, to the fractions of Ni^{3+} and Ni^{4+} cations equal to 56 and 44 %, respectively; this gives the average nickel oxidation state of 3.44+. The latter value is close to 3.54+, the average Ni oxidation state in $LaGa_{0.65}Mg_{0.15}Ni_{0.20}O_{3-\delta}$ equilibrated with air at 298 K, as calculated from TGA results.

B. Oxygen nonstoichiometry

1. Oxygen intercalation processes

For the analysis of defect formation processes, the crystal lattice of $LaGa_{0.65}Mg_{0.15}Ni_{0.20}O_{3-\delta}$ was considered as derived from ideal $A^{3+}B^{3+}O_3^{2-}$ perovskite, where the positively charged point defects include oxygen vacancies ($V_O^{\bullet\bullet}$ in the Kroger-Vink notation) and Ni^{4+} ($Ni_B^{\bullet}$); the negatively charged defects are Mg^{2+} (Mg_B') and Ni^{2+} (Ni_B'). The experimental data presented in this work show that at 973–1223 K, the title composition exhibits a mixed *p*-type electronic and oxygen-ionic conductivity. Respectively, the process of equilibrium oxygen incorporation into the perovskite lattice may be formulated in terms of chemical potentials of gaseous oxygen, vacancies, and electron holes (h)

$$\tfrac{1}{2}\mu(O_2) + \mu(V_O^{\bullet\bullet}) = 2\mu(h), \tag{9}$$

where $\mu(V_O^{\bullet\bullet})$ and $\mu(h)$ are considered with respect to oxygen ions and divalent nickel, respectively [see Eq. (2)].

The generation of electron holes due to oxygen intercalation leads to the formation of Ni^{3+} ($Ni_B^{\times}$) and Ni^{4+} states. Each nickel ion was therefore assumed to form two energetic levels for holes. The Ni^{3+} state corresponds to one localized hole with a ground-level energy (Level 0); the second level (Level 1) is empty in this state. When both levels are filled, Ni^{4+} is formed. The respective hole concentrations are denoted as $[h_{L0}]$ and $[h_{L1}]$, correspondingly. For the total concentration of *p*-type electronic charge carriers

$$[h] = [h_{L0}] + [h_{L1}] = [Ni_B^{\times}] + 2[Ni_B^{\bullet}], \tag{10}$$

where the content of tetravalent nickel is related to oxygen deficiency by the electroneutrality condition

$$[Mg_B'] + [Ni_B'] = [Ni_B^{\bullet}] + 2[V_O^{\bullet\bullet}]. \tag{11}$$

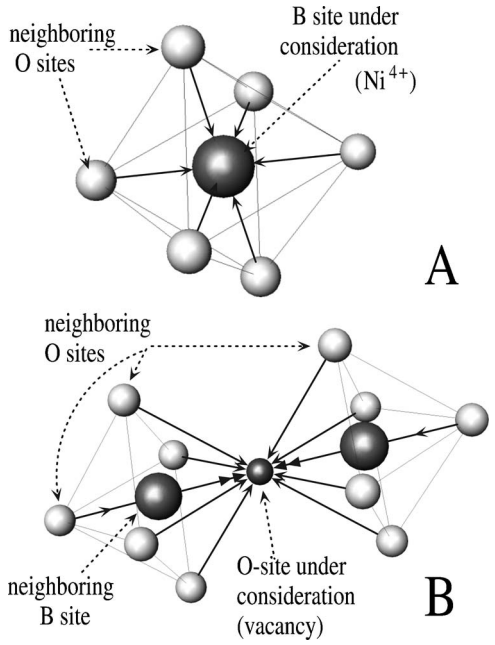

FIG. 7. Structural elements critically affecting the formation of Ni^{4+} cations (a) and oxygen vacancies (b).

In this case, the discrete Fermi-Dirac distribution [Eq. (8)] is expressed as

$$[h_{L0}] = \frac{a(h)[\mathrm{Ni}_\Sigma]}{1 + a(h)}, \tag{12}$$

$$[h_{L1}] = \frac{a(h)[h_{L0}]P_{app}}{\exp\left(\frac{\Delta E_{hh}}{RT}\right) + a(h)}, \tag{13}$$

$$P_{app} = \binom{6}{0}\left(\frac{[V_O^{\bullet\bullet}]}{3}\right)^0\left(1 - \frac{[V_O^{\bullet\bullet}]}{3}\right)^6 = \left(1 - \frac{[V_O^{\bullet\bullet}]}{3}\right)^6, \tag{14}$$

where ΔE_{hh} is the energy difference between Levels 0 and 1, $[\mathrm{Ni}_\Sigma]$ is the total number of nickel cations per unit formula, and P_{app} is the probability of complete occupancy of the oxygen octahedron near a given Ni cation [Fig. 7(a)] when no oxygen vacancy in the nearest neighborhood prevents the localization of two holes due to Coulombic repulsion. In the course of preliminary analysis of the $p(O_2)$-T-δ diagram of $LaGa_{0.65}Mg_{0.15}Ni_{0.20}O_{3-\delta}$, all models neglecting the effect of neighboring oxygen sites were found inadequate. The atomistic computer simulation studies[43] corroborate that, contrary to trivalent B-site cations, the presence of oxygen vacancies near a tetravalent cation in the perovskite lattice is strongly energetically unfavorable. Equations (12)–(14) reflect this limitation, showing that Ni^{2+} and Ni^{3+} are the only states existing in incomplete nickel-oxygen octahedra.

Another important factor affecting the defect equilibria in $LaGaO_3$-based perovskites relates to the association of oxygen vacancies and divalent cations, evidenced by numerous experimental data and atomistic modeling.[11–13,21,44–47] From the energetic point of view, this type of clustering should decrease the vacancy energy. In the case of $LaGa_{0.65}Mg_{0.15}Ni_{0.20}O_{3-\delta}$, all A sites are occupied by lanthanum; no cation ordering was revealed by the XRD analysis. The vacancy energy may hence split, in principle, into three discrete levels formed when zero, one, or two divalent B-site cations are present in the nearest neighborhood [Fig. 7(b)]. On the other hand, Coulombic repulsion forces between positively charged vacancies make it necessary to exclude all configurations with nearest-neighboring vacant sites.[43] This situation can be described as

$$[V_O^{\bullet\bullet}] = a(V_O^{\bullet\bullet})P_{Vapp}\sum_{k=0}^{2}\frac{P'(k,B^{2+})}{\exp\left(\frac{k\Delta E_{VB}}{RT}\right) + a(V_O^{\bullet\bullet})}, \tag{15}$$

where ΔE_{VB} is the difference between the energy levels, and P_{Vapp} is a probability term reflecting the site-exclusion effects near the vacancies and Ni^{4+} cations

$$P_{Vapp} = ([V_O^{\bullet\bullet}] + [O_O^{\times}]) \cdot \left(1 - \frac{[V_O^{\bullet\bullet}]}{3}\right)^{N_{VV}}(1 - [\mathrm{Ni}_B^{\bullet}])^2. \tag{16}$$

The value N_{VV} corresponds to the number of vacancy-neighboring oxygen sites where no other vacancies may exist; $P'(k,B^{2+})$ is the probability of absence of B^{2+} cations, decreasing the oxygen-vacancy energy, in the neighborhood of a given oxygen site

$$P'(k,B^{2+}) = \binom{2}{k}[B^{2+}]^{2-k}(1 - [B^{2+}])^k. \tag{17}$$

In the course of calculations, several versions of N_{VV} and $[B^{2+}]$ were examined. For N_{VV}, these included 8 [first oxygen-coordination sphere, Fig. 7(b)], 10 (all oxygen sites of two nearest B-O octahedra), 12 (nearest neighborhood and 4 sites closest across the O-A-O bonds), and 14 (all listed positions). For the divalent B-site cations, all possible pair and ternary clusters involving Mg^{2+} and Ni^{2+} were tested. The models with $N_{VV}=10$ and $[B^{2+}]=[Mg_B']$ were found most adequate. The latter result seems quite reasonable as all Ni^{2+} are involved in the electron-hole exchange processes, which are much faster than the vacancy migration. The same conclusion was also drawn when analyzing the partial hole conductivity and Seebeck coefficient, as discussed below. Attempts to modify Eqs. (12)–(14) in order to account for Ni^{2+} blocking due to cluster formation resulted in statistically degenerated models.

2. $p(O_2)$-δ-T diagram and defect concentrations

The model for fitting of the experimental data on oxygen nonstoichiometry was formulated on the basis of Eq. (9)

$$\frac{\mu(O_2)}{RT} = -\frac{(2\Delta H_{ex} - h_{O_2}^0) - T(2\Delta S_{ex} - s_{O_2}^0)}{RT} - 2\ln a(V_O^{\bullet\bullet}) + 4\ln a(h), \tag{18}$$

where the chemical potential, standard enthalpy $(h_{O_2}^0)$ and standard entropy $(s_{O_2}^0)$ of gaseous molecular oxygen are defined by IUPAC data,[48] the thermodynamic parameters gov-

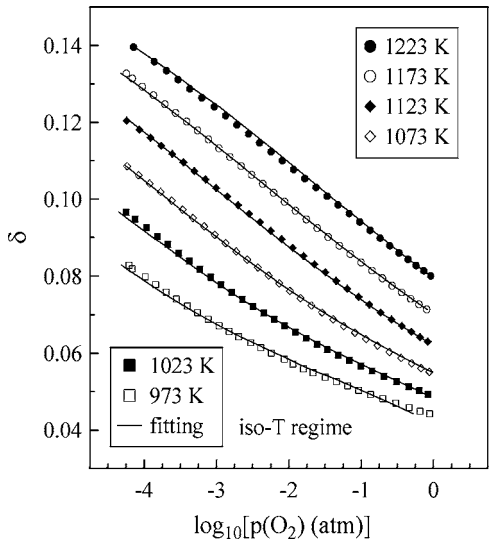

FIG. 8. The $p(O_2)$-δ-T diagram of $LaGa_{0.65}Mg_{0.15}Ni_{0.20}O_{3-\delta}$, measured in the isothermal regime. Solid lines correspond to the fitting results.

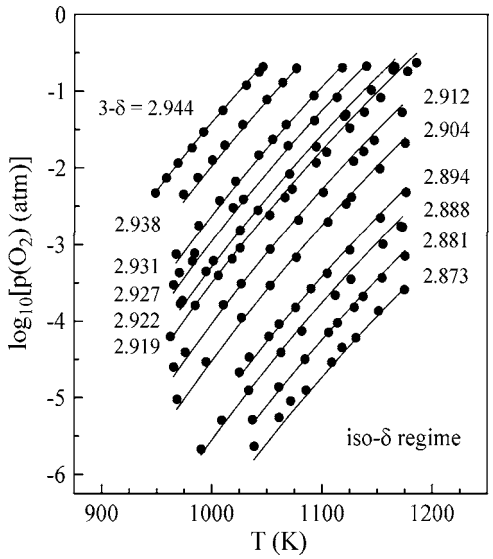

FIG. 9. The $p(O_2)$-δ-T diagram obtained in the iso-nonstoichiometry regime. Solid lines correspond to the fitting results.

erning the oxygen intercalation reaction (ΔH_{ex} and ΔS_{ex}) comprise the concentration-independent part of chemical potentials of oxygen vacancies and holes, and the activities of these defects are expressed by Eqs. (10)–(17). Fitting was performed using the nonlinear regression analysis procedure[49] with $\mu(O_2)/RT$ as a dependent variable; the independent variables included δ and T.

The $p(O_2)$-δ-T diagrams of $LaGa_{0.65}Mg_{0.15}Ni_{0.20}O_{3-\delta}$, determined in the isothermal and isoconcentration regimes, are shown in Figs. 8 and 9, respectively; the solid lines represent fitting results. The regression parameters, including the relative errors and adjusted correlation coefficients, are listed in Table I. The formalism developed in this work provides adequate description of the oxygen content variations. For the $p(O_2)$-δ-T diagrams obtained by two different CT methods, the calculated thermodynamic parameters are very similar, although the use of iso-δ measurement regime results in slightly larger errors. One should also mention that more than 25 alternative models were tested in the course of comparative fitting of the experimental data, including various expressions for chemical potentials of the point defects, site exclusion, and the simplest models derived from the ideal and regular solid solution approximations.[24,27,28] The model consisting of Eqs. (10)–(18) was found most adequate.

Figure 10 presents the calculated concentrations of Ni^{2+}, Ni^{3+}, and Ni^{4+} as a function of oxygen nonstoichiometry and temperature. As expected from average oxidation state calculated by the electroneutrality condition, the concentration of trivalent nickel exhibits a maximum at $\delta \approx 0.08$. Increasing temperature at a constant oxygen deficiency results in lower Ni^{3+} content, reflecting an increasing role of nickel disproportionation. Under most oxidizing conditions when oxygen deficiency is relatively small (δ=0.04–0.05), the concentrations of tri- and tetravalent Ni cations are quite close to each other.

The distribution of oxygen vacancies (Fig. 11) shows a dominant role of the first and zero energy levels, which correspond to the situations when one and two Mg^{2+} cations are present in the vacancy nearest neighborhood, respectively. This finding is in excellent agreement with experimental and computational data on the behavior of Mg-substituted $LaGaO_3$.[13,21,46,47] Due to thermal excitation, increasing temperature leads to a higher population of the second level related to the vacancies surrounded by two trivalent cations. While the concentration of stable ternary Mg'_B-$V^{\bullet\bullet}_O$-Mg'_B clusters is essentially independent of oxygen nonstoichiometry, the occupancy of the first and second energy levels decreases with increasing Ni^{4+} concentration; the latter trend is most pronounced for non-associated vacancies (Level 2).

TABLE I. Parameters of the regression model Eq. (18) for the $p(O_2)$-δ-T diagram.

	Thermodynamic quantities and their errors (95% confidence)				Parameters	
	$\left(\Delta H_{ex}-\frac{1}{2}h^0_{O_2}\right)$, kJ×mol^{-1}	$\left(\Delta S_{ex}-\frac{1}{2}s^0_{O_2}\right)$, J×mol^{-1}×K^{-1}	ΔE_{hh} kJ×mol^{-1}	ΔE_{VB}, kJ×mol^{-1}	Adjusted correlation coefficient	Relative error, %
Iso-T diagram	133.0±0.8	statistically insignificant	14.0±0.5	52.5±0.5	0.9994	0.7
Iso-δ diagram	132±2		9.6±1.3	48.6±1.5	0.999	1.2

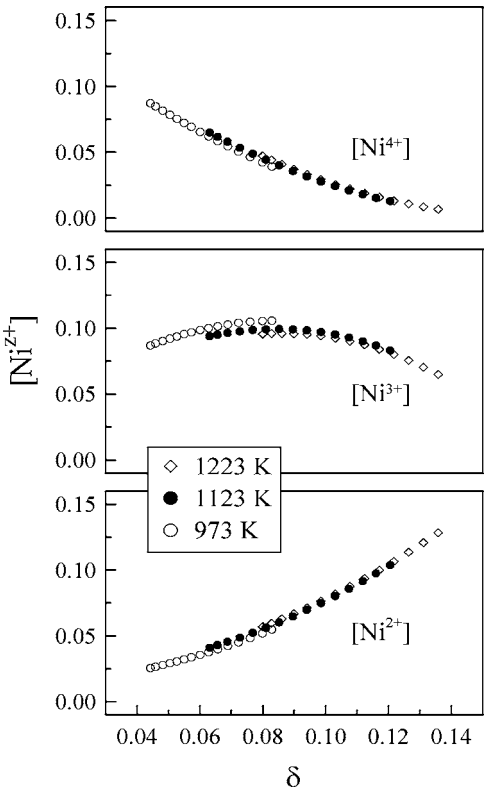

FIG. 10. Calculated concentrations of Ni^{2+}, Ni^{3+}, and Ni^{4+} states in $LaGa_{0.65}Mg_{0.15}Ni_{0.20}O_{3-\delta}$ vs oxygen deficiency.

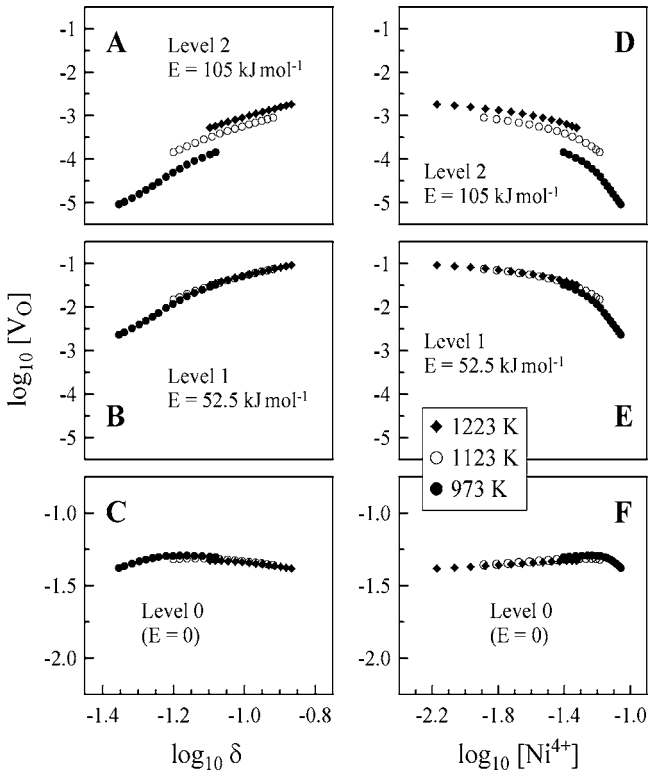

FIG. 11. Oxygen-vacancy distribution between the energy levels as function of the oxygen nonstoichiometry (A–C) and Ni^{4+} content (D–F).

C. Ionic and electronic transport

1. Transport properties vs oxygen pressure and nonstoichiometry

The total conductivity of $LaGa_{0.65}Mg_{0.15}Ni_{0.20}O_{3-\delta}$ in air is predominantly electronic; the oxygen-ion transference number determined by faradaic efficiency technique is 4.3×10^{-2} at 1223 K and decreases to 1.6×10^{-3} at 973 K. Under oxidizing conditions, the conductivity decreases with decreasing $p(O_2)$, Fig. 12. In combination with the faradaic efficiency data and positive sign of the Seebeck coefficient, such a behavior unambiguously indicates prevailing contribution of the *p*-type electronic transport. At oxygen partial pressures lower than 10^{-14}–10^{-9} atm, the $p(O_2)$ dependence of the total conductivity becomes weak, with a slight decrease when the oxygen chemical potential decreases. Very similar tendency is observed for the oxygen content variations in $LaGa_{0.65}Mg_{0.15}Ni_{0.20}O_{3-\delta}$ (upper inset in Fig. 12). On a reduction the oxygen content tends asymptotically to 2.825, the stoichiometric value corresponding to 2+ oxidation state of all nickel cations; the oxygen ionic transport is expected to dominate in these conditions. No evidence of *n*-type electronic conduction was observed. The Seebeck coefficient passes through the minimum in reducing atmospheres, confirming the change in the conductivity regime from dominant *p*-type electronic to ionic. The slope of the α vs $\ln p(O_2)$ dependencies at oxygen chemical potentials below the minima is close to $-R/4F$, the value typical for pure oxygen-ionic conductors.[50]

Figure 13 shows the temperature dependence of hole mobility (u_h) calculated using the definition[27,51]

$$\sigma_p = e[h]\cdot u_h \frac{N_{UC}}{V_{UC}}, \tag{19}$$

where the hole concentration is determined from oxygen nonstoichiometry by the electroneutrality condition, the values of partial *p*-type electronic conductivity (σ_p) are extracted from the faradaic efficiency and total conductivity data as explained below, N_{UC} is the number of formula units per unit cell, and V_{UC} is the unit cell volume. The mobility has a temperature-activated character, thus confirming that possible delocalization effects can be neglected. Due to relatively isolated state of nickel cations surrounded mainly by Ga^{3+} and Mg^{2+}, the values of u_h are low, typical for a small-polaron mechanism.[27,52] Oxygen intercalation in the perovskite structure increases the mobility, which can be attributed to the lattice contraction and to increasing concentration of Ni-O-Ni bonds governing hole transport. The latter factors may also contribute to the observed decrease in the hole mobility activation energy (inset in Fig. 13). At the same time, the apparent activation energy values are rather high for a simple small-polaron hopping, suggesting the relevance of the site-exclusion effects.

2. Partial conductivities

The total conductivity of $LaGa_{0.65}Mg_{0.15}Ni_{0.20}O_{3-\delta}$ (Fig. 12) was analyzed as a sum of the *p*-type electronic and oxygen-ionic (σ_{ion}) contributions, both $p(O_2)$ dependent

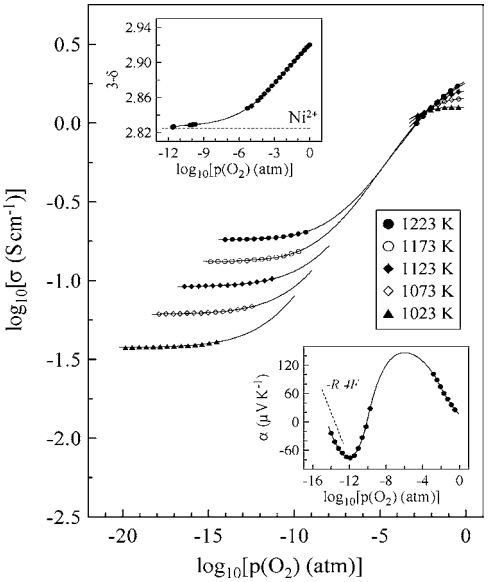

FIG. 12. Oxygen partial pressure dependence of the total conductivity of $LaGa_{0.65}Mg_{0.15}Ni_{0.20}O_{3-\delta}$. The insets illustrate variations of the oxygen content ($3-\delta$) and Seebeck coefficient (α) vs oxygen partial pressure at 1223 K. Solid lines are for visual guidance only.

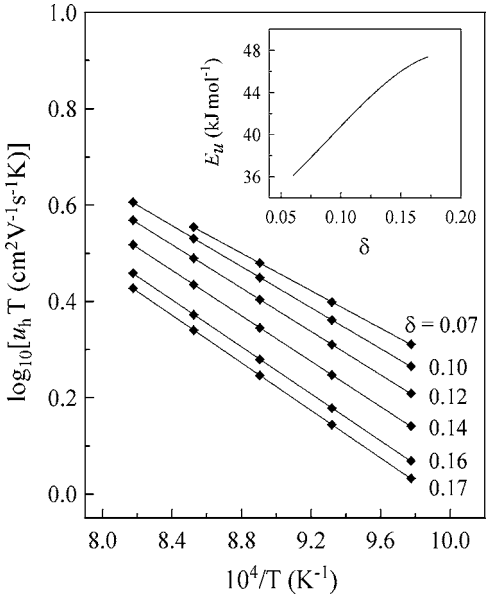

FIG. 13. Temperature dependence of the hole mobility in $LaGa_{0.65}Mg_{0.15}Ni_{0.20}O_{3-\delta}$ at fixed oxygen nonstoichiometry. The inset shows variations of the hole mobility activation energy vs oxygen deficiency.

$$\sigma = \sigma_{\text{ion}} + \sigma_p. \tag{20}$$

At atmospheric oxygen pressure, these contributions were separated by the faradaic efficiency measurements; the results were then combined with σ vs $p(O_2)$ and δ vs $p(O_2)$ dependencies for fitting. The models for the partial ionic and hole conductivities were based on the random-walk theory[13,27,51,52] and extended to account for defect interactions.

For the perovskite lattices where all oxygen sites are energetically equivalent, the random-walk theory predicts[13,27]

$$\sigma_{\text{ion}} = \frac{B_0 l^2 (2F)^2 \nu_{\text{O}}}{RT}\left(1 - \frac{[V_{\text{O}}^{\bullet\bullet}]}{3}\right)\frac{[V_{\text{O}}^{\bullet\bullet}]}{3} c_{\text{O}} \exp\left(-\frac{E_{\text{ion}}}{RT}\right), \tag{21}$$

where l is the distance between two nearest-neighbor sites, ν_{O} is the ion-jump attempt frequency, c_{O} is the site density, and B_0 is a constant comprising geometrical factors and entropic terms. The effective activation energy for ionic transport, E_{ion}, is a sum of the vacancy-migration and association enthalpies.[13] In the case of $LaGa_{0.65}Mg_{0.15}Ni_{0.20}O_{3-\delta}$, the concentration of oxygen vacancies is significantly lower than that of oxygen ions, $[V_{\text{O}}^{\bullet\bullet}]/3 \ll 1$ (Fig. 8). Also, under reducing and moderately oxidizing conditions, the fraction of vacant sites between two trivalent cations is low and cannot be considered as the transport-determining factor (Fig. 11); the number of vacancies trapped between two divalent cations is essentially independent of the oxygen chemical potential and temperature. The relationship between ionic conductivity and vacancy concentration can therefore be formulated as

$$\sigma_{\text{ion}} = \frac{A_0}{T} P_{V\text{jump}} \exp\left(-\frac{E_{\text{ion}}}{RT}\right) \tag{22}$$

with the probability term

$$P_{V\text{jump}} = \binom{11}{1}\frac{[V_{\text{O}}^{\bullet\bullet}]}{3}\left(1 - \frac{[V_{\text{O}}^{\bullet\bullet}]}{3}\right)^{N_{VV}}, \tag{23}$$

where A_0 is constant comprising a vacancy-blocking factor. As for Eq. (16), the latter equation accounts for the vacancy repulsion. However, the site-exclusion effect near Ni^{4+} was found statistically insignificant and, thus, is neglected. Such difference in behavior may be associated with several factors, primarily energetic. First of all, the electrostatic attraction forces between Ni^{4+} and neighboring O^{2-} may impede an anion jump towards a vacancy. This phenomenon would be reflected by an increase in the activation energy and a slight decrease in the mobile ions concentration. The latter factor may hardly be distinguished statistically from the ionic conductivity data, since the concentration of tetravalent nickel at elevated temperatures is much lower compared to the total oxygen content (Fig. 10). In contrast, preliminary analysis of the $\sigma_{\text{ion}}=f(\delta,T)$ dependencies showed a clear increase in the activation energy with increasing oxygen content, probably contributed also by the long-range Coulombic repulsion between positively charged $V_{\text{O}}^{\bullet\bullet}$ and $Ni_{\text{B}}^{\bullet}$. Hence, Eq. (22) was further modified by introducing one extra factor in the exponential term

$$\sigma_{\text{ion}} = \frac{A_0}{T} P_{V\text{jump}} \exp\left(-\frac{E_{\text{ion}}}{RT} - \frac{[Ni_{\text{B}}^{\bullet}]}{[Ni_{\Sigma}]}\frac{E_{\text{Ni}}}{RT}\right), \tag{24}$$

where $[Ni_{\text{B}}^{\bullet}]/[Ni_{\Sigma}]$ is the fraction of Ni^{4+} cations, and E_{Ni} is the additive energy associated with these Coulombic interactions.

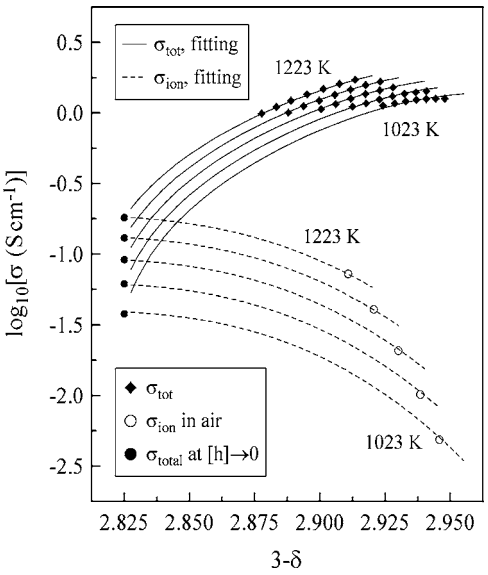

FIG. 14. Dependence of the total and partial oxygen-ionic conductivities on oxygen content at 1023–1223 K (the experimental data are given with the step of 50 K). Solid and dashed lines correspond to fitting results (see text).

The partial *p*-type electronic conductivity via a hopping mechanism can be described using a similar formalism[27,51,52]

$$\sigma_p = A_h P_{h\text{jump}} \exp\left(-\frac{E_h}{RT}\right), \tag{25}$$

where A_h and E_h are the preexponential factor and activation energy, respectively. The hole-jump probability ($P_{h\text{jump}}$) comprises three terms

$$P_{h\text{jump}} = P_V \times (P_{\text{L0}} + P_{\text{L1}}), \tag{26}$$

where P_{L0} and P_{L1} correspond to the jumps from the lower and higher energy levels (Levels 0 and 1), respectively

$$P_{\text{L0}} = [\text{Ni}_\text{B}^\times]([\text{Ni}_\text{B}^\times] + [\text{Ni}_\text{B}']) \exp\left(-\frac{\Delta E_{hh}}{RT}\right), \tag{27}$$

$$P_{\text{L1}} = [\text{Ni}_\text{B}^\bullet]([\text{Ni}_\text{B}^\times] + [\text{Ni}_\text{B}']). \tag{28}$$

The activation energy increment, ΔE_{hh}, is equal to the hole-hole interaction energy calculated from the thermodynamic data (Table I). As oxygen vacancies break the Ni-O-Ni bonds and may also increase energetic barrier due to distortions of the nickel-oxygen polyhedra, the corresponding site-exclusion effects are taken into account by introducing third probability term

$$P_V = \binom{11}{0}\left(\frac{[V_\text{O}^{\bullet\bullet}]}{3}\right)^0\left(1-\frac{[V_\text{O}^{\bullet\bullet}]}{3}\right)^{11} = \left(1-\frac{[V_\text{O}^{\bullet\bullet}]}{3}\right)^{11}. \tag{29}$$

Equations (10), (11), (20), and (24)–(29) form a regression model to describe the total, oxygen-ionic and *p*-type electronic conductivities of $LaGa_{0.65}Mg_{0.15}Ni_{0.20}O_{3-\delta}$. The fitting results are in good agreement with experimental data (Fig. 14), thus confirming validity of the formalism described above. The regression parameters are listed in Table II. Notice that the calculated E_{ion} value is very close to the activation energies for oxygen-ionic transport in the Ni-free LSGM materials with similar content of acceptor-type cations.[11,13]

TABLE II. Parameters of the regression models for partial conductivities. Note: R_{adj} is the adjusted correlation coefficient.

Oxygen-ion conductivity, Eq. (24)		Hole conductivity, Eq. (25)	
A^0, S×K×cm^{-1}	$(1.4\pm0.5)\times10^6$	A^h, S×cm^{-1}	$(2.4\pm0.2)\times10^3$
E_{ion}, kJ/mol	89±1	E_h, kJ/mol	24.3±0.8
E_{Ni}, kJ/mol	29.6±0.9		
R_{adj}	0.9998	R_{adj}	0.996

3. Seebeck coefficient

The Seebeck coefficient of a mixed ionic-electronic conductor comprises the contributions of all charge carriers, multiplied by the corresponding transference numbers.[53,54] In case of $LaGa_{0.65}Mg_{0.15}Ni_{0.20}O_{3-\delta}$

$$\alpha = t_\text{O}\alpha_\text{O} + (1-t_\text{O})\alpha_p \tag{30}$$

with α_O and α_p being the partial thermopower of oxygen ions and holes, respectively. If equilibrium with gas phase is achieved and Soret effects are negligible, the partial ionic thermopower may be formulated as[50,54]

$$\alpha_\text{O} = -\frac{R}{4F}\ln p(\text{O}_2) + \frac{1}{4F}\left[s^0_{\text{O}_2} - 2\left(\bar{S}_{\text{O}^{2-}} + \frac{q_{\text{O}^{2-}}}{T}\right)\right], \tag{31}$$

where $S^0_{\text{O}_2}$ is the standard molar entropy of gaseous oxygen, $\bar{S}_{\text{O}^{2-}}$ is the partial molar entropy of mobile oxygen ions, and $q_{\text{O}^{2-}}$ is the heat transported by these ions. Analogously, the partial hole thermopower is expressed via the partial molar entropy and transported heat of the *p*-type electronic charge carriers ($\bar{S}_h$ and q_h, respectively)[51,52,55]

$$\begin{aligned}\alpha_p &= \frac{R}{F}\left(\bar{S}_\text{h} + \frac{q_\text{h}}{RT}\right) \\ &= \frac{R}{F}\ln\left(\frac{[\text{Ni}_\Sigma]!}{[h_{\text{L0}}]!([\text{Ni}_\Sigma]-[h_{\text{L0}}])!}\cdot\frac{[h_{\text{L0}}]!}{[h_{\text{L1}}]!([h_{\text{L0}}]-[h_{\text{L1}}])!}\right) \\ &\quad + \frac{q_h}{FT}.\end{aligned} \tag{32}$$

Using Stirling's approximation, one can obtain

$$\alpha_p = \frac{R}{F}\left(\ln\frac{[\text{Ni}_\Sigma]-[h_{\text{L0}}]}{[h_{\text{L1}}]} + \frac{q_h}{RT}\right). \tag{33}$$

The latter term, which can be estimated from the temperature dependence of the partial thermopower at fixed charge-carrier concentration, is very low and typically can be neglected.[52] For the holes occupying zero energy level, the number of states may, in principle, deviate from $[\text{Ni}_\Sigma]$ due to an additional site-exclusion effect resulting from the formation of defect clusters involving Ni^{2+} and oxygen vacancies.

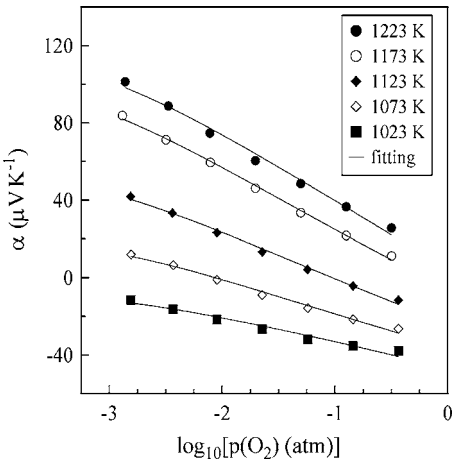

FIG. 15. Oxygen partial pressure dependence of the Seebeck coefficient of $LaGa_{0.65}Mg_{0.15}Ni_{0.20}O_{3-\delta}$. Solid lines correspond to the fitting results.

In order to verify negligible role of such clustering, Eq. (33) was rewritten

$$\alpha_p = \frac{R}{F} \ln \frac{[B_\Sigma] - [h_{L0}]}{[h_{L1}]}. \tag{34}$$

The model comprising Eqs. (30), (31), and (34) were used for fitting the $\alpha - \ln[p(O_2)]$ dependencies (Fig. 15), with $\left(\bar{S}_{O^{2-}} + \frac{q_{O^{2-}}}{T}\right)$ and $[B_\Sigma]$ as the regression parameters. Since ionic contribution to the total conductivity under oxidizing conditions is relatively low (Fig. 14), the partial molar entropy of oxygen ions was considered constant; the variations in $\bar{S}_{O^{2-}}$ cannot be distinguished statistically. Despite this simplification, the fitting results shown as solid lines in Fig. 15 are in excellent agreement with experimental data. The estimated number of states, $[B_\Sigma]$, is 0.21 ± 0.02 at 1023–1223 K. Within the limits of experimental uncertainty, these values are equal to the number of nickel cations per $LaGa_{0.65}Mg_{0.15}Ni_{0.20}O_{3-\delta}$ unit formula, thus providing an additional proof to the statistical-thermodynamic model presented in this work.

V. CONCLUSIONS

The $p(O_2)$-δ-T diagram of perovskite-type $LaGa_{0.65}Mg_{0.15}Ni_{0.20}O_{3-\delta}$ was determined at 923–1223 K in the oxygen partial pressure range 5×10^{-5} to 0.9 atm by coulometric titration and thermogravimetry. The oxygen nonstoichiometry values indicate the coexistence of Ni^{2+}, Ni^{3+}, and Ni^{4+} oxidation states, which is probably associated with a strong dilution of nickel ions surrounded by the constant-valence cations including acceptor-type Mg^{2+}. The presence of Ni^{4+} was confirmed by the magnetic susceptibility measurements and by the analysis of oxygen intercalation processes, *p*-type electronic conductivity and Seebeck coefficient at 1023–1223 K. The defect thermodynamics and transport in Ni-substituted lanthanum gallate are strongly affected by point-defect interactions, in particular the Coulombic repulsion between oxygen vacancies and/or electron holes and the vacancy association with Mg^{2+} cations. These factors were analyzed using a statistical thermodynamic approach, introducing the point-defect interaction energy in the concentration-dependent part of defect chemical potentials and accounting for the site-exclusion effects. The relationships between defect concentrations and chemical potentials were expressed by the discrete Fermi-Dirac distribution, where the corresponding number of states is determined by the configurational probabilities assessed via binomial distributions. Although further studies are necessary to identify exact state of *p*-type electronic charge carriers, the high-temperature defect formation processes can be adequately described assuming that each nickel cation may provide one or two energetic levels for the hole location, depending on the occupancy of nearest-neighboring oxygen sites. The level of oxygen-vacancy mobility is significantly influenced by site exclusion near positively charged vacancies and by the height of energetic barrier for ion jumps, which increases with increasing average Ni oxidation state.

ACKNOWLEDGMENTS

This work was supported by the FCT, Portugal (projects POCI/CTM/59197/2004 and BPD/11606/2002) and the NATO Science for Peace program (project 978002). Experimental contributions and helpful discussions, made by A. Shaula and A. Viskup, are gratefully acknowledged.

*Corresponding author. Fax: +351-234-425300. Electronic address: kharton@cv.ua.pt

[1] T. J. Mazanec, R. Prasad, R. Odegard, C. Steyn, and E. T. Robinson, Stud. Surf. Sci. Catal. **136**, 147 (2001).

[2] A. Julbe, D. Farrusseng, and C. Guizard, Catal. Today **104**, 102 (2005).

[3] A. Thursfield and I. A. Metcalfe, J. Mater. Chem. **14**, 2475 (2004).

[4] S. Pei, M. S. Kleefisch, T. P. Kobylinski, J. Faber, C. A. Udovich, V. Zhang-McCoy, B. Dabrowski, U. Balachandran, R. L. Mieville, and R. B. Poeppel, Catal. Lett. **30**, 201 (1995).

[5] M. Schwartz, J. H. White, and A. F. Sammels, US Patent 6214757 (2001).

[6] T. Ishihara and Y. Takita, Catal. Surv. Jpn. **4**, 125 (2000).

[7] T. Ishihara, Y. Tsuruta, T. Todaka, H. Nishiguchi, and Y. Takita, Solid State Ionics **152-153**, 709 (2002).

[8] A. L. Shaula, A. A. Yaremchenko, V. V. Kharton, D. I. Logvinovich, E. N. Naumovich, A. V. Kovalevsky, J. R. Frade, and F. M. B. Marques, J. Membr. Sci. **221**, 69 (2003).

[9] A. A. Yaremchenko, V. V. Kharton, E. N. Naumovich, D. I. Shestakov, V. F. Chukharev, A. V. Kovalevsky, A. L. Shaula, M. V. Patrakeev, J. R. Frade, and F. M. B. Marques, Solid State

Ionics **177**, 549 (2006).
[10] T. Ishihara, H. Matsuda, M. A. bin Bustam, and Y. Takita, Solid State Ionics **86-88**, 197 (1996).
[11] P. Huang and A. Petric, J. Electrochem. Soc. **143**, 1644 (1996).
[12] J. W. Stevenson, T. R. Armstrong, D. E. McCready, I. R. Pederson, and W. J. Weber, J. Electrochem. Soc. **144**, 3613 (1997).
[13] K. Huang, R. S. Tichy, and J. B. Goodenough, J. Am. Ceram. Soc. **81**, 2565 (1998).
[14] T. Ishihara, T. Shibayama, H. Nishiguchi, and Y. Takita, J. Mater. Sci. **36**, 1125 (2001).
[15] B. Gharbage, R. T. Baker, and F. M. B. Marques, J. Mater. Sci. Lett. **17**, 75 (1998).
[16] K. Yamaji, H. Negishi, T. Horita, N. Sakai, and H. Yokokawa, Solid State Ionics **135**, 389 (2000).
[17] N. Trofimenko and H. Ullmann, Solid State Ionics **118**, 215 (1999).
[18] N. J. Long, F. Lecarpentier, and H. L. Tuller, J. Electroceram. **3**, 399 (1999).
[19] J. W. Stevenson, K. Hasinska, N. L. Canfield, and T. R. Armstrong, J. Electrochem. Soc. **147**, 3213 (2000).
[20] V. V. Kharton, A. A. Yaremchenko, A. P. Viskup, G. C. Mather, E. N. Naumovich, and F. M. B. Marques, J. Electroceram. **7**, 57 (2001).
[21] V. V. Kharton, A. P. Viskup, A. A. Yaremchenko, R. T. Baker, B. Gharbage, G. C. Mather, F. M. Figueiredo, E. N. Naumovich, and F. M. B. Marques, Solid State Ionics **132**, 119 (2000).
[22] A. A. Yaremchenko, A. L. Shaula, D. I. Logvinovich, V. V. Kharton, A. V. Kovalevsky, E. N. Naumovich, J. R. Frade, and F. M. B. Marques, Mater. Chem. Phys. **82**, 684 (2003).
[23] M. V. Patrakeev, E. B. Mitberg, A. A. Lakhtin, I. A. Leonidov, V. L. Kozhevnikov, V. V. Kharton, M. Avdeev, and F. M. B. Marques, J. Solid State Chem. **167**, 203 (2002).
[24] S. Ling, Phys. Rev. B **49**, 864 (1994).
[25] S. Ling, Solid State Ionics **70-71**, 686 (1994).
[26] S. Ling, J. Phys. Chem. Solids **55**, 1445 (1994).
[27] V. N. Chebotin, *Physical Chemistry of Solids* (Khimiya, Moscow, 1982).
[28] M. H. R. Lankhorst, H. J. M. Bouwmeester, and H. Verweij, J. Am. Ceram. Soc. **80**, 2175 (1997).
[29] I. A. Leonidov, V. L. Kozhevnikov, E. B. Mitberg, M. V. Patrakeev, V. V. Kharton, and F. M. B. Marques, J. Mater. Chem. **11**, 1201 (2001).
[30] V. V. Kharton, A. P. Viskup, E. N. Naumovich, and N. M. Lapchuk, Solid State Ionics **104**, 67 (1997).
[31] V. V. Kharton, A. L. Shaula, N. P. Vyshatko, and F. M. B. Marques, Electrochim. Acta **48**, 1817 (2003).
[32] L. A. Chick, L. R. Pederson, G. D. Maupin, J. L. Bates, L. E. Thomas, and G. L. Exarhos, Mater. Lett. **10**, 6 (1990).
[33] K. Yamaji, T. Horita, M. Ishikawa, N. Sakai, and H. Yokokawa, Solid State Ionics **121**, 217 (1999).
[34] M. Stanislowski, U. Seeling, D.-H. Peck, S.-K. Woo, L. Singheiser, and K. Hilpert, Solid State Ionics **176**, 2523 (2005).
[35] M. V. Patrakeev, E. B. Mitberg, A. A. Lakhtin, and I. A. Leonidov, Ionics **4**, 191 (1998).
[36] V. N. Tikhonovich, O. M. Zharkovskaya, E. N. Naumovich, I. A. Bashmakov, V. V. Kharton, and A. A. Vecher, Solid State Ionics **160**, 259 (2003).
[37] V. V. Kharton, A. A. Yaremchenko, and E. N. Naumovich, J. Solid State Electrochem. **3**, 303 (1999).
[38] J. A. Alonso, M. J. Martínez-Lope, and M. A. Hidalgo, J. Solid State Chem. **116**, 146 (1995).
[39] D. Reinen, U. Kesper, and D. Belder, J. Solid State Chem. **116**, 355 (1995).
[40] A. Manthiram, J. P. Tang, and V. Manivannan, J. Solid State Chem. **148**, 499 (1999).
[41] I. Saadoune, M. Ménétrier, and C. Delmas, J. Mater. Chem. **7**, 2505 (1997).
[42] I. Saadoune and C. Delmas, J. Solid State Chem. **136**, 8 (1998).
[43] E. N. Naumovich, M. V. Patrakeev, V. V. Kharton, M. S. Islam, A. A. Yaremchenko, J. R. Frade, and F. M. B. Marques, Solid State Ionics **177**, 457 (2006).
[44] M. M. Günter, H. Boysen, C. Corte, M. Lerch, and E. Suard, Z. Kristallogr. **220**, 218 (2005).
[45] M. S. Islam, P. R. Slater, J. R. Tolchard, and T. Dinges, Dalton Trans. **2** 3061 (2004).
[46] M. S. Islam, J. Mater. Chem. **10**, 1027 (2000).
[47] M. S. Islam and R. A. Davies, J. Mater. Chem. **14**, 86 (2004).
[48] IUPAC, Commission on Thermodynamics, *Oxygen, International Thermodynamic Tables of the Fluid State—9* (Blackwell Scientific Publications, Oxford, 1987).
[49] N. R. Draper and H. Smith, *Applied Regression Analysis* (John Wiley and Sons, New York, 1981).
[50] E. Ahlgren and F. W. Poulsen, Solid State Ionics **70-71**, 528 (1994).
[51] P. Kofstad, *Nonstoichiometry, Diffusion and Electrical Conductivity in Binary Metal Oxides* (Wiley-Interscience, New York, 1972).
[52] J. B. Goodenough, in *Conduction in Low-Mobility Materials*, edited by N. Klein, D. S. Tannhauser, and M. Pollak (Taylor and Francis, London, 1971), p. 87.
[53] C. Wagner, Prog. Solid State Chem. **7**, 1 (1972).
[54] S. Yamaguchi, K. Kobayashi, K. Abe, S. Yamazaki, and Y. Iguchi, Solid State Ionics **113-115**, 393 (1998).
[55] P. M. Chaikin, and G. Beni, Phys. Rev. B **13**, 647 (1976).